Supplement of Atmos. Chem. Phys., 23, 5233–5249, 2023
https://doi.org/10.5194/acp-23-5233-2023-supplement

Atmospheric Chemistry and Physics
Open Access
EGU

Supplement of

Toward a versatile spaceborne architecture for immediate monitoring of the global methane pledge

Yuchen Wang et al.

Correspondence to: Pengfei Li (lpf_zju@163.com), Shaocai Yu (shaocaiyu@zju.edu.cn), and Yuqing Pan (panyuqing@hebau.edu.cn)

S1. Uncertainty analysis for the PRISMA-based methane retrievals

The PRISMA-based methane retrievals can present systematic and random errors. At first glance via the top-of-atmosphere radiance at 2300 nm (Fig. S5), the cases in the Rumaila (Iraq) and Hassi Messaoud (Algeria) fields represent a preferable condition with a bright and homogeneous surface feature, while the cases in the Burgan (Kuwait) and Wattenberg (the United States) fields represent a challenging condition because of a relatively dark and heterogeneous surface. By comparison, the case in Yangquan (China) is even more challenging, in which mountainous areas exist. In the most cases (except for the case in Fig. 1d4), the methane plumes are clearly uncorrelated with the surface brightness from space.

We thus evaluate their performance using end-to-end simulations, as shown in previous studies. First, the ideal plumes are prescribed via the large-eddy-driven Weather and Research Forecasting Model (the WRF-Chem-LES model) (Varon et al., 2018). The key configuration includes common wind fields (i.e., 3.5 m/s), high resolution (i.e., 30 ×30 m^2), and constant emission rates (e.g., 500, 1000, and 1500 kg/h). On this basis, uncorrelated noises with random increments are then added. They represent the expected instrument precision presenting normal distributions with zero mean biases and standard deviations of 1 ~ 5 %. Second, the enhancements of volume mixing ratios are converted into two-way spectral atmospheric transmittance. The calculation basis includes air mass factors based on the real observation zenith angles, vertical profiles of dry air column densities, and methane absorption cross-section data. These three data come from the satellite instrument records, ERA5 reanalysis dataset, and the HIgh-resolution TRANSmission molecular absorption (HITRAN2016) database. Third, the subsequent transmittance spectra are convolved with the PRISMA-based spectral responses and then multiplied by the original PRISMA top-of-atmosphere radiance spectrums. To prevent across-track variations in spectral calibration, we perform such processes on a per-column basis. Finally, the resulting PRISMA-based top-of-atmosphere radiance images are processed with the same matched-filter algorithm over the cases explored in this work.

Figure S9 shows the resulting retrieval errors. Such errors denote not only those caused by surface structures via absorption features of SWIR bands but also those due to random measurement noise. They are indicated by probability distribution functions generated by running the retrieval over a simulated image devoid of methane plumes (i.e., emission rate equal to 0 kg/h). As a result, we find that these errors roughly flow Gaussian distributions, likely due to the fact that random noise, rather than systematic noise driven by surface structures, and thus dominate the whole errors. This again indicates a strong dependence of the retrieval error and subsequent plume detection limit on the surface feature.

Figure S10 represents more quantitative uncertain analysis for the retrieval performance. For each case, the input $\Delta\mathbf{XCH4}$ maps are compared with the output $\Delta\mathbf{XCH4}$ retrievals. Methane retrieval results via the WRF-Chem-LES simulations and associated biases are presented in Table S3. Overall, they are sketchily consistent in terms of the slopes. The retrieval method performs the best for most of the cases, with a substantial number of pixels above the noise level, while more dispersed scatters are found in the Yangquan case (Fig. 1g2). The root mean squared errors (RMSE) could be controlled within the range of 37 ~

127 ppb. Collectively, we do not observe systematic errors in this instrument and our algorithm (Fig. S6 and Figs. S10 and S11).

S2. Uncertainty analysis for the TROPOMI-based methane emission estimates

We provide independent emission estimates for the TROPOMI-based methane hotspots using the WRF-Chem model. On this basis, the differences between the WRF-Chem-based and IME-based results reflect the intrinsic uncertainties in the IME method. The WRF simulation is nudged to National Centers for Environmental Prediction final analysis data at 0.25° × 0.25° spatial resolution and six-hour temporal resolution. For each hotspot, the model is performed at 5 × 5 km^2 horizontal resolution over a 50 × 50 km^2 domain. The boundary condition is obtained from the CAMS reanalysis dataset. Note that the inner domain does not feedback with the outer domain (i.e., so-called one-way nested simulations). The grid-specific methane emissions are originally taken from the bottom-up emission inventories (EDGARv6.0). Other general configurations could be found in our previous studies(Wang et al., 2020, 2021).

Methane emissions are estimated via the Bayesian inverse solution which optimizes a single state vector **x** as:

$$\hat{\mathbf{x}} = \mathbf{x_A} + \mathbf{S_A}\mathbf{K}^{\boldsymbol{T}}(\mathbf{K}\mathbf{S_A}\mathbf{K}^{\boldsymbol{T}} + \mathbf{S_C})^{-\mathbf{1}}(\mathbf{y} - \mathbf{K}\mathbf{x_A}), \text{ (Eq. 6)}$$

where $\hat{\mathbf{x}}$ is the optimized state vector containing individual elements for daily emissions as well as daily background concentrations; $\mathbf{x_A}$ is the prior taken as the mean reported emission rate from the bottom-up emission inventories; **K** is the Jacobian constructed by running perturbation simulations for the state vector element; $\mathbf{S_A}$ is the prior error covariance matrix using 100% error for the emissions and 10% for the boundary conditions; **y** contains the TROPOMI observations; and $\mathbf{S_C}$ is the observational error covariance matrix using as error the standard deviation of the difference between the prior model and the observations (20 ppb).

Because of uncertainties in meteorology, the WRF output sometime before or after the observation time can give a better simulation of the scene. Hence, we sample model simulations one hour before and after the optimal time at 15-min time intervals. To ensure that small mismatches between the locations in the simulated and TROPOMI-based hotspots do not lead to underestimated emissions, we then average TROPOMI pixels together on a 3 × 3 grid before the inversion and estimate the observational error following the central limit theorem (i.e. dividing by $\sqrt{\mathbf{n}}$ where **n** is the number of observations).

The IME method can also be constrained by the WRF-Chem-based wind fields. On this basis, the subsequent TROPOMI-based methane emission estimates could be compared with the original IME-based results (i.e., driven by the ERA5 reanalysis data). The resulting differences would reflect the impacts of the wind data on the IME-based methane emission estimates.

Table S2 summarizes the differences in the methane emission estimates from these two different methods. The results from the WRF-Chem model are consistently lower than those from the IME method in an acceptable range (23 ~ 39%). Such divergencies could be narrowed to a large extent (17 ~ 34%) once the wind data in these two methods are unified to the WRF-Chem-based wind fields. This indicates the noticeable impacts of wind information on the IME method. Besides, we also find the inevitable uncertainties in the complex physical functions in the WRF-Chem model. A representative is that the WRF-

Chem-based results account for the wind direction that, in contrast, is not considered in the IME method. From this analysis, we conclude that the TROPOMI-based methane emission estimates based on the IME method are reliable, the errors of which could be controlled within -40% (Table S2).

S3. Uncertainty analysis for the PRISMA-based methane emission estimates

We provide independent emission estimates for the PRISMA-based methane plumes using the WRF-Chem-LES model (Irakulis-Loitxate et al., 2021). The differences between the WRF-CHEM-LES-based and IME-based results reflect the intrinsic uncertainties in the IME method. For each plume, this model is conducted at 30×30 m^2 horizontal resolution over a 3×3 km^2 domain. This resolution and domain size allow the placement and resolving of the individual plume and keep the computational and storage costs at a reasonable level. Each simulation has 121 vertical levels, with ~ 3 m for the first three layers and ~10 m for the upper layers up to the model top at 2 km height. The terrain information in the inner domain is obtained from the United States Geological Survey (http://ned.usgs.gov/) at 1/3 arc-second (~10 m) resolution representative of the areas where the methane plumes are active. The boundary condition is obtained from a regional CTM (the two-way coupled WRF-CMAQ model) simulation with 3×3 km^2 horizontal resolution over a 12×12 km^2 domain. Other configurations are shown in our previous results (Mehmood et al., 2020; Wang et al., 2020, 2021). Note that the inner domain does not feedback with the outer domain (i.e., so-called one-way nested simulations). This configuration would not affect our results as the simulated plumes would not touch the boundaries of the inner domain. Each simulation is performed for five hours. The first three hours serve as a spin-up period, while the rest two hours are used for analysis. The time step for the inner domain is 0.1 s, and instantaneous values are saved every second (i.e., every ten time-steps). Confidence intervals are obtained from the t-statistic calculated every 5 minutes during the simulation, starting from 15 minutes before and ending 15 minutes after the satellite overpass.

For each plume, its nominal emission magnitude is assumed to be 1000 kg/h. On this basis, the emission magnitude is scaled by matching the total mass of excess methane in the simulated plume. The specific grids that the plume covered are defined using the "contourLines" function of R with a custom threshold (i.e., 2.5% of the total mass of excess methane, corresponding to the variance of the scene-based methane retrieval). The identified grids would not be sensitive to the configuration of the threshold due to the sharp plume edge. Meanwhile, the local background is defined within 1 km of the emission source. Finally, we adjust the scale factor to best match the area-integrated total mass of excess methane of the observed plume. On this basis, the WRF-Chem-LES-based emission estimates are achieved. Collectively, the differences between the WRF-Chem-LES-based and IME-based results reflect the intrinsic uncertainties in the IME method.

Table S3 presents the summary of the results. Overall, such differences could be controlled within -70%. Such divergencies are also mainly contributed by the differences in the wind fields between the WRF-LES-based results and the ERA5 reanalysis dataset. Yet, since all of the wind information is model product, we cannot know if the WRF-LES-based results are more

reliable than the ERA5 reanalysis data. In theory, we could project that the WRF-LES-based results at a higher resolution might have a better performance.

The IME method can also be constrained by the WRF-Chem-LES-based wind fields. On this basis, the subsequent PRISMA-based methane emission estimates could be compared with the original IME-based results (i.e., driven by the ERA5 reanalysis data). The resulting differences would reflect the impacts of the wind data on the IME-based methane emission estimates. As shown in Table S3, such differences reach up to -49%, which is within the precision errors of the IME method, as illustrated above. Besides, the comparison of the IME-based and WRF-Chem-LES results driven by the same simulated wind fields demonstrated that there are also strong uncertainties in the particular methane emission estimating method. Such uncertainties have an impact as high as that from the wind fields and, still, are not beyond uncertainties in the IME method.

Collectively, the results verify large methane emissions as reported in this work. The associated uncertainties are mainly due to wind fields and intrinsic model errors and can be controlled within -70%. It should be noted that our uncertain analysis might be only suitable for the cases in this work and more quantitative assessments based on the WRF-LES model are necessary to be promoted widely.

S4. Uncertainty analysis for other sources

Note that such quantitative estimates of the errors are close to previous findings but might be unsuitable worldwide, especially for those occurring in more complex conditions. We thus expect that, as our framework is promoted, there is a profound need to conduct more WRF-Chem-LES simulations to investigate the performance of our framework in as many and as complex environments as possible.

Besides, the second tier of our framework observes strong methane vestiges (i.e., likely plume tails) above the storage tanks in the Burgan field. We require to confirm that such vestiges are caused by the real plumes or the technical noises due to the surface albedo perturbations. As abovementioned, the latter has been corrected in the matched-filtered algorithm used in the second tier of our framework. To make our results more persuasive, we retrieve the PRISMA-based $\mathbf{\Delta XCH_4}$ together with surface albedo from just two spectral measurements, one featuring methane absorption (i.e., 2300 nm) and one not (i.e., 1700 nm). These two adjacent spectral bands have similar surface and aerosol reflectance properties but differ in their methane absorption properties. Specifically, we utilize these two spectral bands to launch the matched-filtered algorithm separately. The differences in the results would, in principle, eliminate surface albedo effects and thus isolate the signals of the methane plumes. Figure S5 shows that the 2300 nm-driven matched-filtered algorithm results in noticeable methane vestiges above the storage tanks, while the 1700 nm-driven algorithm does not. Therefore, we could infer that such signals may very well led by real methane plumes rather than technical noises, although on-site measurements are absent. Similar multi-spectral techniques have been widely used to retrieve signals of methane plumes from ground-based (Innocenti et al., 2017), airborne (Leifer et al., 2006; Roberts et al., 2010), and satellite-based (Ehret et al., 2021; Varon et al., 2021) remote sensing instruments.

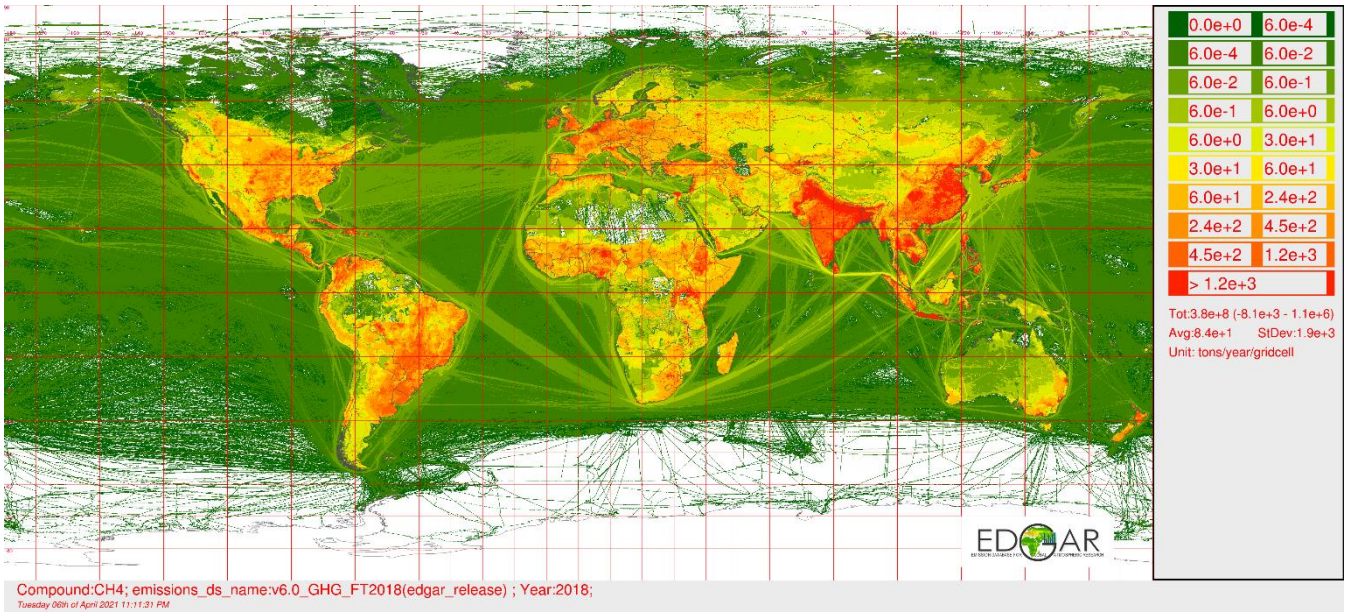

Fig. S1. A state-of-the-art global methane emission map for 2018(Janssens-Maenhout et al., 2019)**.** The map was obtained from the EDGARv6.0 dataset (https://edgar.jrc.ec.europa.eu/gallery?release=v60ghg&substance=CH4&sector=TOTALS) (Last access: February 1, 2022).

Fig. S2. Attributions of the PRISMA-based methane plumes to specific plants or infrastructures. The subpanels successively correspond to the plumes in Figs. 1b1 ~ 1g2. For each plume, the map is zoomed to the maximum for visual inspections. The overpass times of the satellites are also presented. The base maps are obtained from © Google Map.

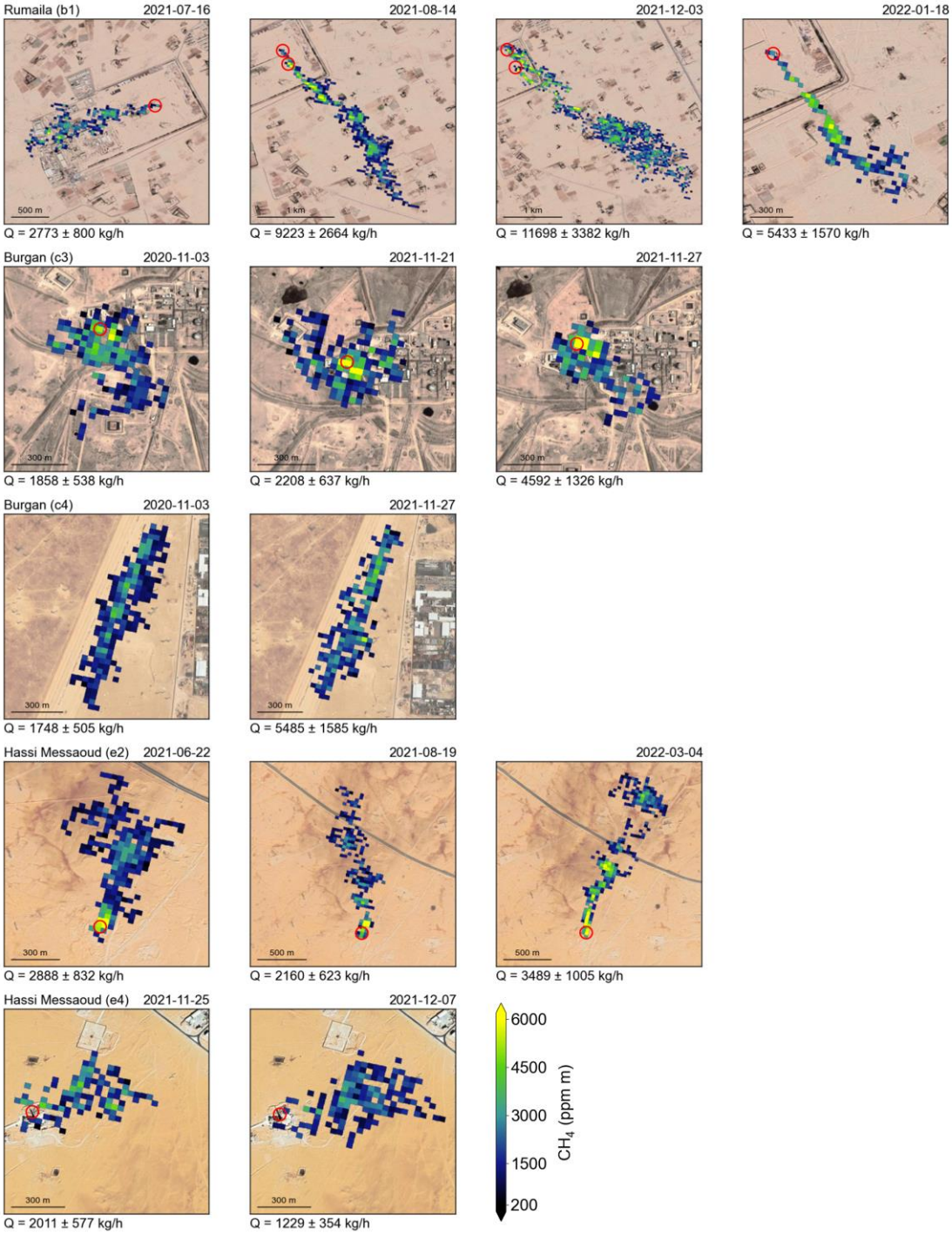

135

136 **Fig. S3. The same as Figs. 1b1, c3, c4, e2, and e4 but the sampling window of the second-tiered monitoring is extended.**
137 On this basis, more representatives are presented. The base maps are obtained from © Google Map. Plume sources in the
138 PRISMA-based results are marked by red circles.

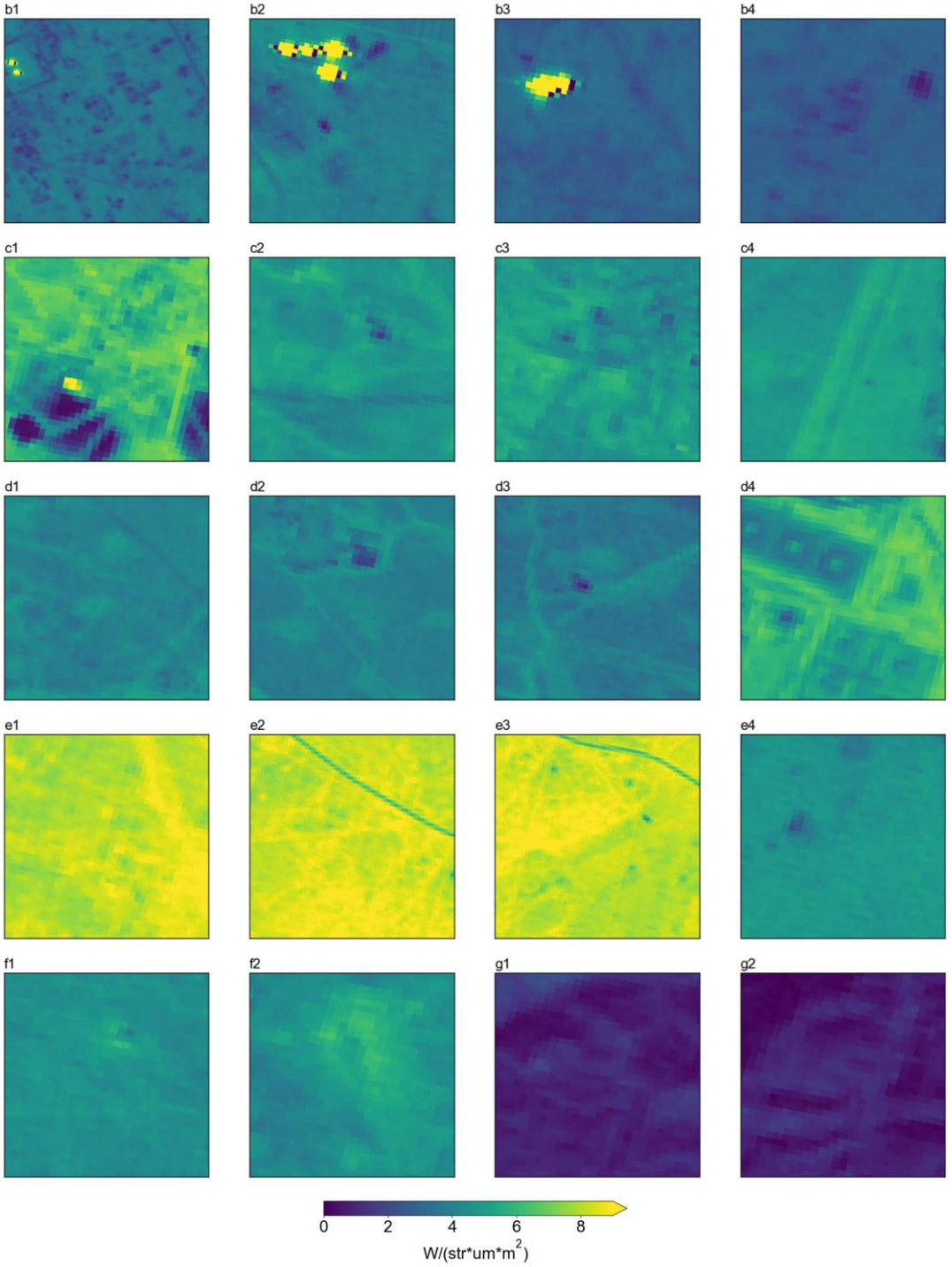

Fig. S4. Maps of top-of-atmospheric radiance at 2300 nm for the methane plumes as shown in Figs. 1b ~ 1f. The small panels confirm that spatial distributions of methane plumes were clearly uncorrelated with those of surface brightness.

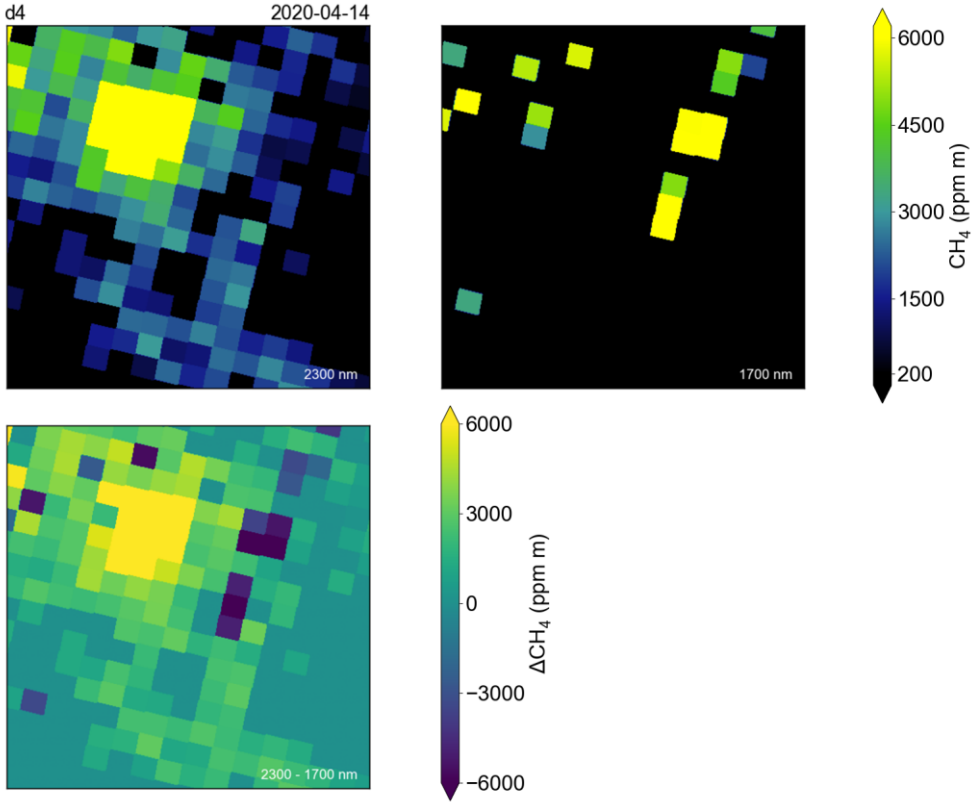

Fig. S5. Methane vestiges above the storage tanks in the Burgan field retrieved by (a) 1700 nm- and (b) 2300 nm -driven matched-filtered algorithms. Their differences highlight the suspect methane leakage from the storage tanks (c).

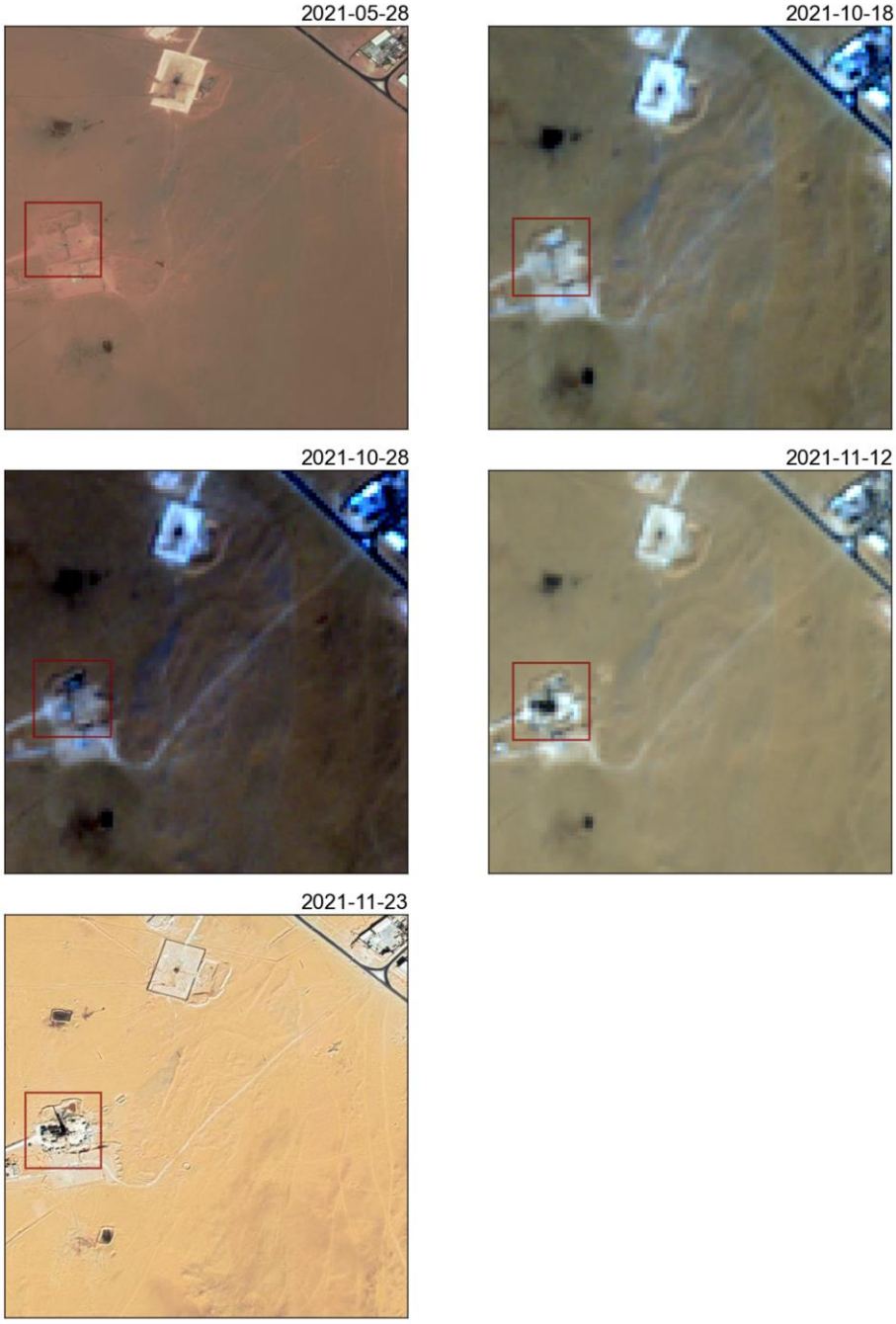

Fig. S6. Historical maps of methane plumes in the Hassi Messaoud field (Fig. 1e4). The satellite images for October 18th, October 28th, and November 12th are obtained from the Sentinel-2 images, while others © Google Map. The red rectangle marks the new methane super-emitter.

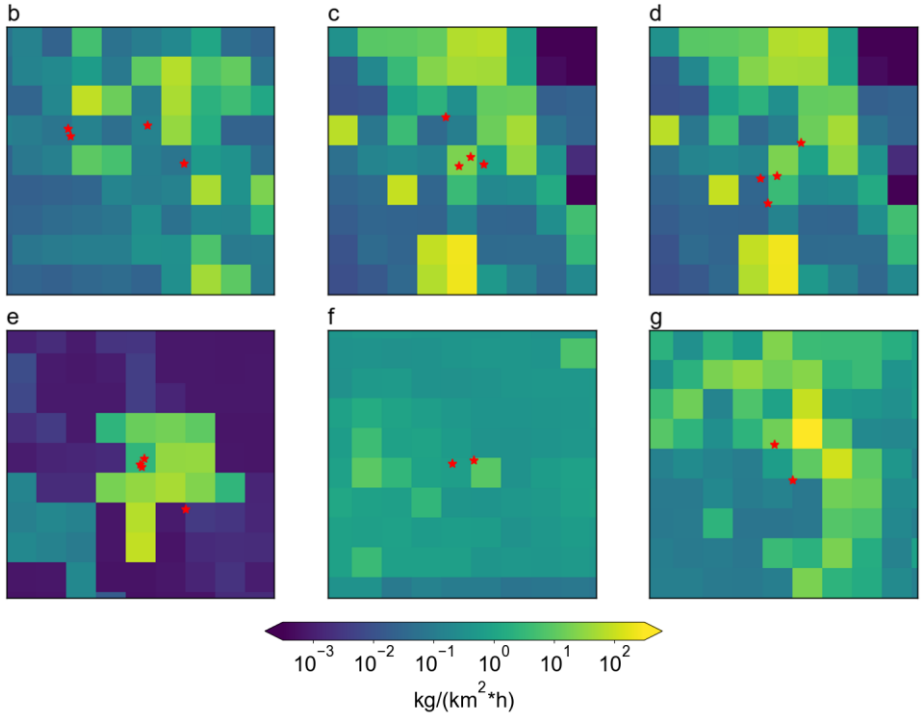

Fig. S7. Spatial distributions of methane emissions in bottom-up emission inventories. The panels successively correspond to the regions in Figs. 1b ~ 1g. The five-pointed stars correspond to the black dots in Fig. 1a.

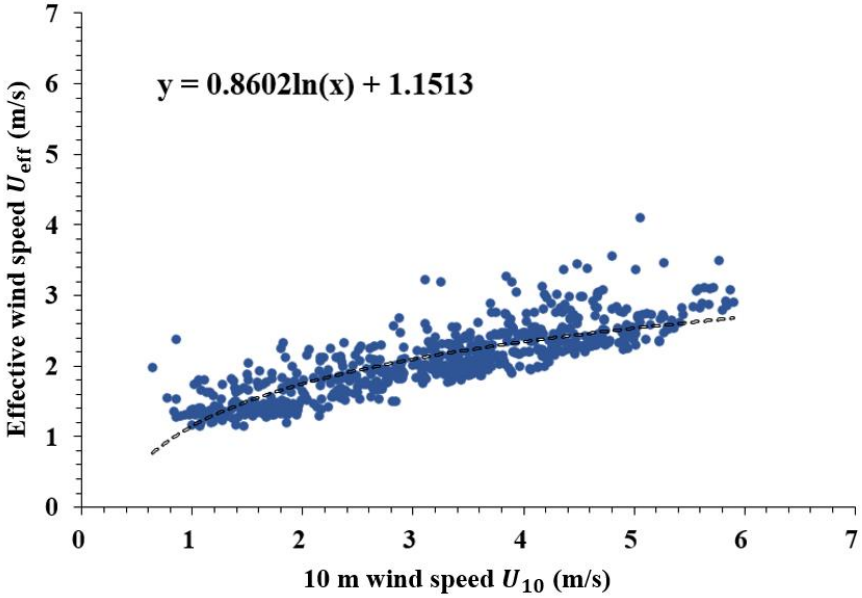

Fig. S8. Relationship between the effective (U_{eff}) and 10-m (U_{10}) wind speeds in the second-tiered monitoring. The LES plumes assuming 5% instrument precision.

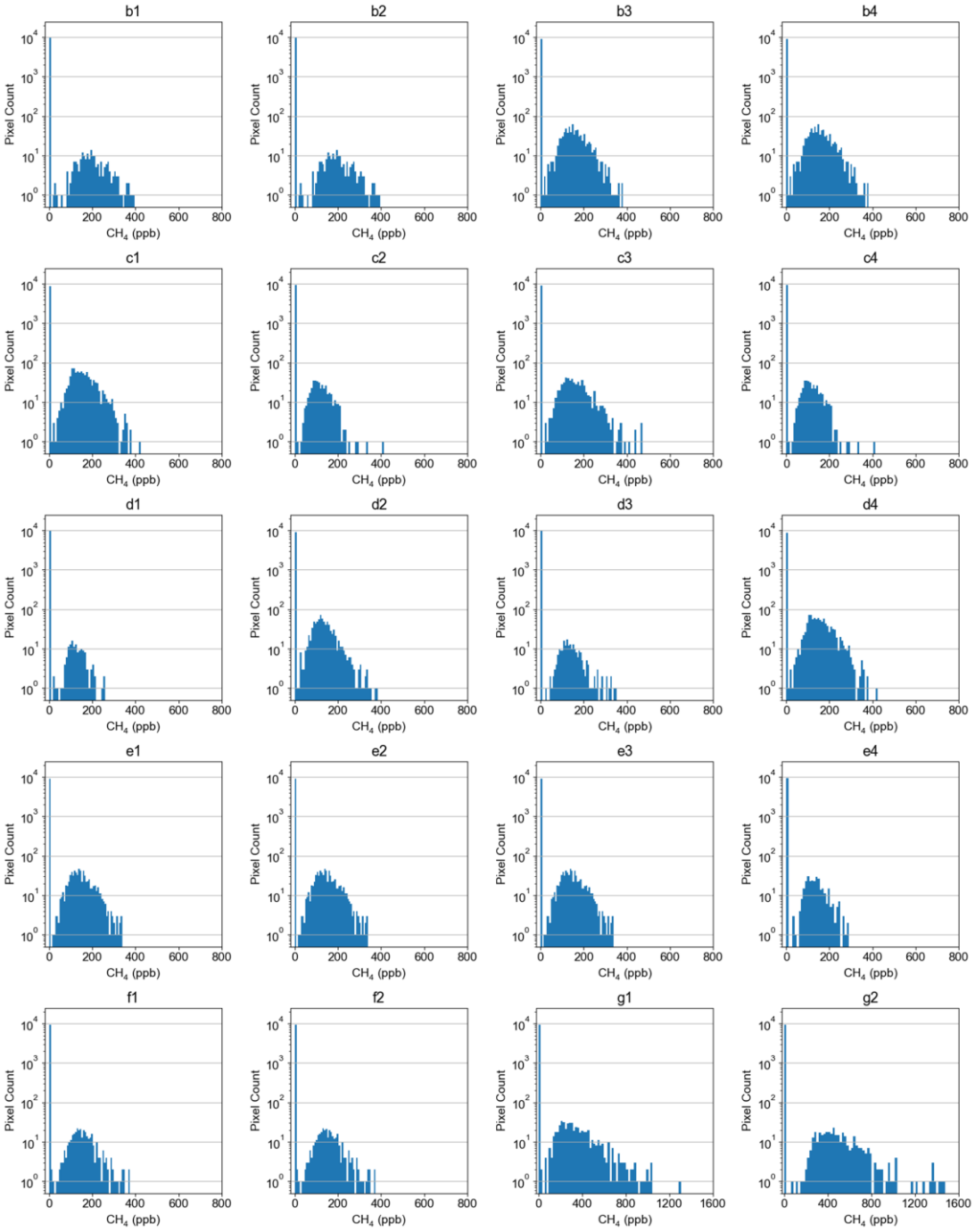

Fig. S9. Histograms of the retrieved ΔXCH4 inside the selected 100 × 100 subset areas over the detected methane super-emitters for the no-plume cases. The μ and σ values represent the mean and standard deviation of the distributions, respectively. A Gaussian curve has been fitted to each distribution.

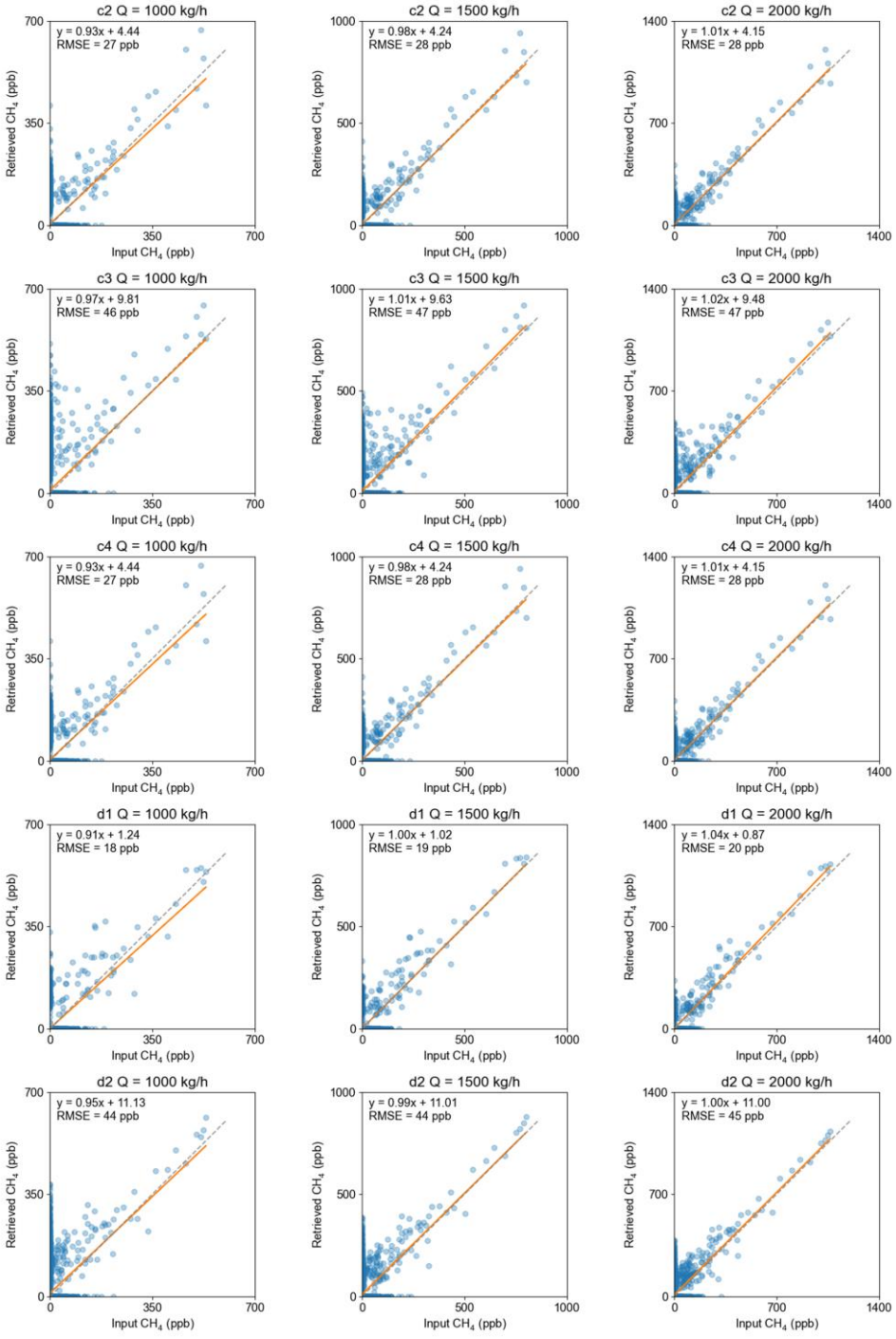
c2 Q = 1000 kg/h
y = 0.93x + 4.44
RMSE = 27 ppb
c2 Q = 1500 kg/h
y = 0.98x + 4.24
RMSE = 28 ppb
c2 Q = 2000 kg/h
y = 1.01x + 4.15
RMSE = 28 ppb
c3 Q = 1000 kg/h
y = 0.97x + 9.81
RMSE = 46 ppb
c3 Q = 1500 kg/h
y = 1.01x + 9.63
RMSE = 47 ppb
c3 Q = 2000 kg/h
y = 1.02x + 9.48
RMSE = 47 ppb
c4 Q = 1000 kg/h
y = 0.93x + 4.44
RMSE = 27 ppb
c4 Q = 1500 kg/h
y = 0.98x + 4.24
RMSE = 28 ppb
c4 Q = 2000 kg/h
y = 1.01x + 4.15
RMSE = 28 ppb
d1 Q = 1000 kg/h
y = 0.91x + 1.24
RMSE = 18 ppb
d1 Q = 1500 kg/h
y = 1.00x + 1.02
RMSE = 19 ppb
d1 Q = 2000 kg/h
y = 1.04x + 0.87
RMSE = 20 ppb
d2 Q = 1000 kg/h
y = 0.95x + 11.13
RMSE = 44 ppb
d2 Q = 1500 kg/h
y = 0.99x + 11.01
RMSE = 44 ppb
d2 Q = 2000 kg/h
y = 1.00x + 11.00
RMSE = 45 ppb
Retrieved CH4 (ppb)
Input CH4 (ppb)

164

165

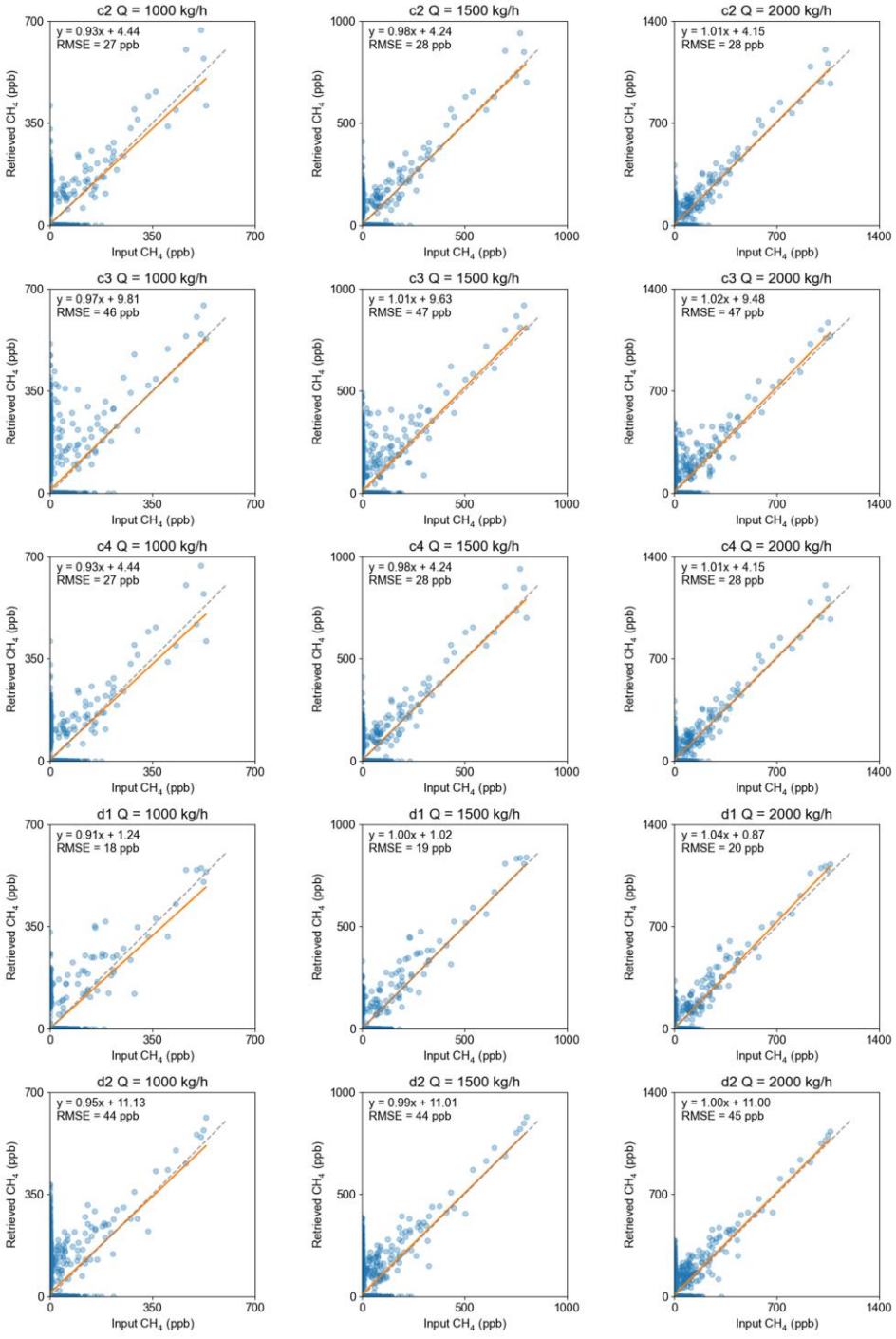
c2 Q = 1000 kg/h
y = 0.93x + 4.44
RMSE = 27 ppb
c2 Q = 1500 kg/h
y = 0.98x + 4.24
RMSE = 28 ppb
c2 Q = 2000 kg/h
y = 1.01x + 4.15
RMSE = 28 ppb
c3 Q = 1000 kg/h
y = 0.97x + 9.81
RMSE = 46 ppb
c3 Q = 1500 kg/h
y = 1.01x + 9.63
RMSE = 47 ppb
c3 Q = 2000 kg/h
y = 1.02x + 9.48
RMSE = 47 ppb
c4 Q = 1000 kg/h
y = 0.93x + 4.44
RMSE = 27 ppb
c4 Q = 1500 kg/h
y = 0.98x + 4.24
RMSE = 28 ppb
c4 Q = 2000 kg/h
y = 1.01x + 4.15
RMSE = 28 ppb
d1 Q = 1000 kg/h
y = 0.91x + 1.24
RMSE = 18 ppb
d1 Q = 1500 kg/h
y = 1.00x + 1.02
RMSE = 19 ppb
d1 Q = 2000 kg/h
y = 1.04x + 0.87
RMSE = 20 ppb
d2 Q = 1000 kg/h
y = 0.95x + 11.13
RMSE = 44 ppb
d2 Q = 1500 kg/h
y = 0.99x + 11.01
RMSE = 44 ppb
d2 Q = 2000 kg/h
y = 1.00x + 11.00
RMSE = 45 ppb
Retrieved CH4 (ppb)
Input CH4 (ppb)

166

167

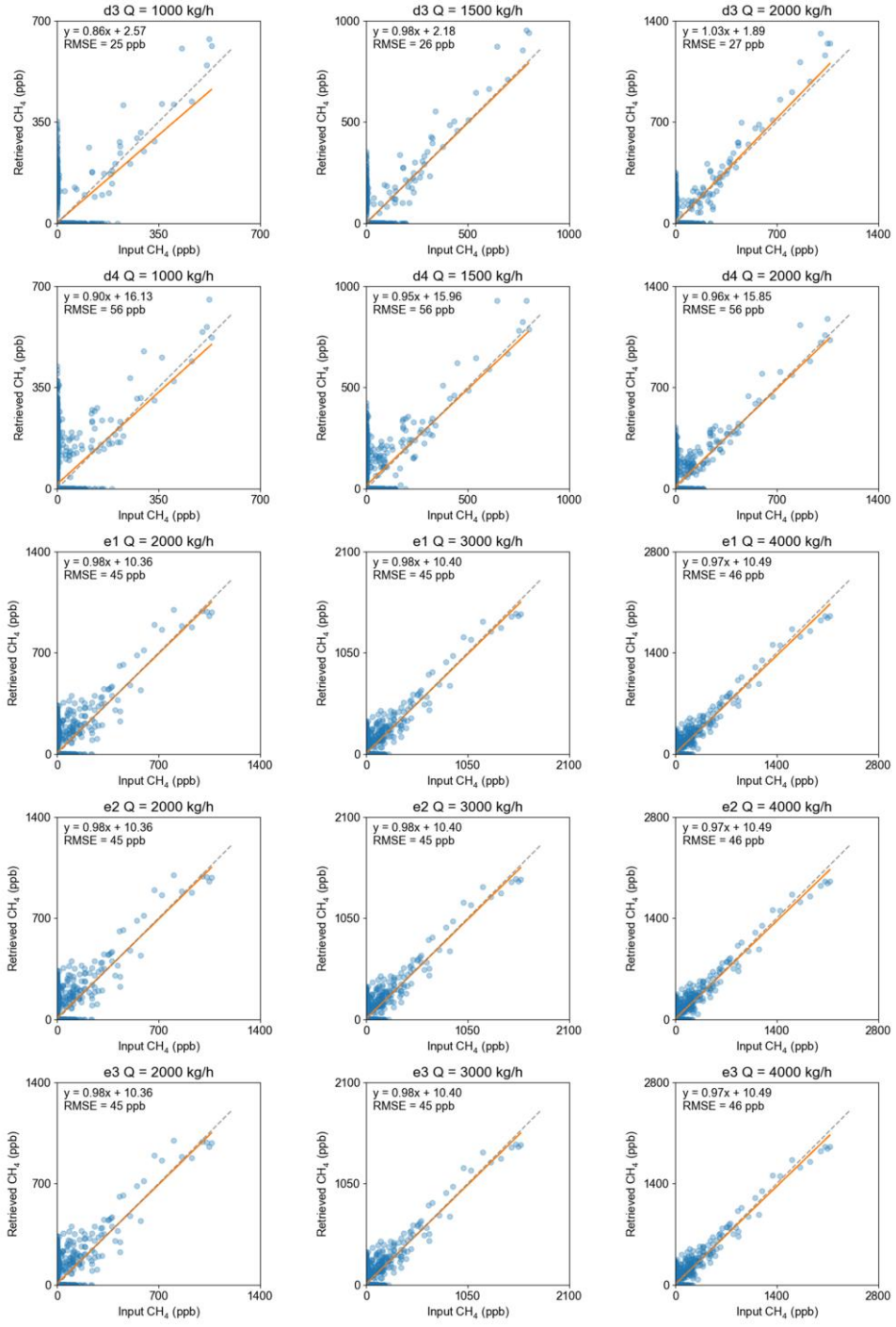

Fig. S10. Scatter plots of the input and retrieved ΔXCH4 for the simulations over the methane super-emitters. The dash and red lines represent the 1:1 line and fitted linear model, respectively.

Table S1. Summary of methane hotspots and associated super-emitters via our multi-tiered, space-based framework. Their emission rates, precision errors, locations (latitude and longitude), and corresponding figure panels are shown.

Regions	Figure panels	Latitude (°)	Longitude (°)	Emission rates kg/h	Uncertainties kg/h
Rumaila	b	30.300	47.580	46138	17580
Rumaila	b1	30.291	47.725	11698	7416
Rumaila	b2	30.416	47.604	5053	3961
Rumaila	b3	30.406	47.336	6569	4009
Rumaila	b4	30.382	47.345	1510	722
Burgan	c	29.000	48.000	7873	3509
Burgan	c1	28.980	47.989	1378	992
Burgan	c2	29.013	48.027	1543	831
Burgan	c3	29.145	47.943	1858	1408
Burgan	c4	28.988	48.072	1748	804
Burgan	d	29.000	48.000	6332	3954
Burgan	d1	28.947	47.978	1375	1067
Burgan	d2	28.855	47.946	3576	1495
Burgan	d3	28.940	47.921	4425	2653
Burgan	d4	29.058	48.057	3593	2541
Hassi Messaoud	e	31.780	6.000	127676	59470
Hassi Messaoud	e1	31.798	6.012	2757	1297
Hassi Messaoud	e2	31.779	5.998	2160	1108
Hassi Messaoud	e3	31.769	6.003	4326	2453
Hassi Messaoud	e4	31.628	6.151	1229	862
Wattenberg	f	40.430	-104.380	4805	2201
Wattenberg	f1	40.443	-104.341	2023	867
Wattenberg	f2	40.430	-104.412	1142	486
Yangquan	g	37.800	113.520	33594	16918
Yangquan	g1	37.746	113.551	7616	4413
Yangquan	g2	37.866	113.489	4382	2034

Table S2. Comparison of the TROPOMI-based methane emission estimates between the IME and WRF-Chem method.

Figure	IME (kg/h)	WRF-Chem (kg/h)	IME-Wind* (kg/h)	(WRF-Chem - IME)/IME (%)	(IME-Wind - IME)/IME (%)
b	46138	32758	36449	-29	-21
c	7873	5117	5589	-35	-29
d	6332	3863	4179	-39	-34
e	127676	77882	105971	−39	-17
f	4805	3700	4036	-23	-16
g	33594	23516	24859	-30	-26

*IME-Wind: the wind data in the IME method is constrained by the WRF-Chem model.

Table S3. Comparison of the PRISMA-based methane emission estimates between the IME and WRF-Chem-LES method.

Figure	IME (kg/h)	WRF-Chem-LES (kg/h)	IME-Wind* (kg/h)	(WRF-Chem-LES - IME)/IME (%)	(IME-Wind - IME)/IME (%)
b1	11698	5381.08	6784.84	-54	-42
b2	5053	1869.61	3840.28	-63	-24
b3	6569	3021.74	4926.75	-54	-25
b4	1510	815.4	906	-46	-40
c1	1378	454.74	1005.94	-67	-27
c2	1543	972.09	972.09	-37	-37
c3	1858	743.2	873.26	-60	-53
c4	1748	1136.2	1293.52	-35	-26
d1	1375	467.5	756.25	-66	-45
d2	3576	2467.44	2717.76	-31	-24
d3	4425	2566.5	3363	-42	-24
d4	3593	1113.83	1832.43	-69	-49
e1	2757	1792.05	1847.19	-35	-33
e2	2160	1188	1576.8	-45	-27
e3	4326	2509.08	2811.9	-42	-35
e4	1229	516.18	749.69	-58	-39
f1	2023	1456.56	1537.48	-28	-24
f2	1142	787.98	833.66	-31	-27
g1	7616	4569.6	5483.52	-40	-28
g2	4382	2935.94	3067.4	-33	-30

*IME-Wind: the wind data in the IME method is constrained by the WRF-Chem model.

Reference.

Ehret, T., Truchis, A. De, Mazzolini, M., Morel, J.-M., d'Aspremont, A., Lauvaux, T., Duren, R., Cusworth, D. and Facciolo, G.: Global Tracking and Quantification of Oil and Gas Methane Emissions from Recurrent Sentinel-2 Imagery, 2021.

Innocenti, F., Robinson, R., Gardiner, T., Finlayson, A. and Connor, A.: Differential Absorption Lidar (DIAL) Measurements of Landfill Methane Emissions, Remote Sens. , 9(9), doi:10.3390/rs9090953, 2017.

Irakulis-Loitxate, I., Guanter, L., Liu, Y.-N., Varon, D. J., Maasakkers, J. D., Zhang, Y., Chulakadabba, A., Wofsy, S. C., Thorpe, A. K., Duren, R. M. and Others: Satellite-based survey of extreme methane emissions in the Permian basin, Sci. Adv., 7(27), eabf4507, doi:10.1126/sciadv.abf4507, 2021.

Janssens-Maenhout, G., Crippa, M., Guizzardi, D., Muntean, M., Schaaf, E., Dentener, F., Bergamaschi, P., Pagliari, V., Olivier, J. G. J., Peters, J. A. H. W., van Aardenne, J. A., Monni, S., Doering, U., Petrescu, A. M. R., Solazzo, E. and Oreggioni, G. D.: EDGAR v4.3.2 Global Atlas of the three major greenhouse gas emissions for the period 1970–2012, Earth Syst. Sci. Data, 11(3), 959–1002, doi:10.5194/essd-11-959-2019, 2019.

Leifer, I., Roberts, D., Margolis, J. and Kinnaman, F.: In situ sensing of methane emissions from natural marine hydrocarbon seeps: A potential remote sensing technology, Earth Planet. Sci. Lett., 245(3), 509–522, doi:https://doi.org/10.1016/j.epsl.2006.01.047, 2006.

Mehmood, K., Wu, Y., Wang, L., Yu, S., Li, P., Chen, X., Li, Z., Zhang, Y., Li, M., Liu, W., Wang, Y., Liu, Z., Zhu, Y., Rosenfeld, D. and Seinfeld, J. H.: Relative effects of open biomass burning and open crop straw burning on haze formation over central and eastern China: Modeling study driven by constrained emissions, Atmos. Chem. Phys., 20(4), doi:10.5194/acp-20-2419-2020, 2020.

Roberts, D. A., Bradley, E. S., Cheung, R., Leifer, I., Dennison, P. E. and Margolis, J. S.: Mapping methane emissions from a marine geological seep source using imaging spectrometry, Remote Sens. Environ., 114(3), 592–606, doi:https://doi.org/10.1016/j.rse.2009.10.015, 2010.

Varon, D. J., Jacob, D. J., McKeever, J., Jervis, D., Durak, B. O. A., Xia, Y. and Huang, Y.: Quantifying methane point sources from fine-scale satellite observations of atmospheric methane plumes, Atmos. Meas. Tech., 11(10), 5673–5686, doi:10.5194/amt-11-5673-2018, 2018.

Varon, D. J., Jervis, D., McKeever, J., Spence, I., Gains, D. and Jacob, D. J.: High-frequency monitoring of anomalous methane point sources with multispectral Sentinel-2 satellite observations, Atmos. Meas. Tech., 14(4), 2771–2785, doi:10.5194/amt-14-2771-2021, 2021.

Wang, L., Yu, S., Li, P., Chen, X., Li, Z., Zhang, Y., Li, M., Mehmood, K., Liu, W., Chai, T., Zhu, Y., Rosenfeld, D. and Seinfeld, J. H.: Significant wintertime PM2.5 mitigation in the Yangtze River Delta, China from 2016 to 2019: observational constraints on anthropogenic emission controls, Atmos. Chem. Phys. Discuss., 2020, 1–31, doi:10.5194/acp-2020-510, 2020.

Wang, L., Chen, X., Zhang, Y., Li, M., Li, P., Jiang, L., Xia, Y., Li, Z., Li, J., Wang, L., Hou, T., Liu, W., Rosenfeld, D., Zhu, T., Zhang, Y., Chen, J., Wang, S., Huang, Y., Seinfeld, J. H. and Yu, S.: Switching to electric vehicles can lead to significant reductions of PM2.5 and NO2 across China, One Earth, 4(7), 1037–1048, doi:https://doi.org/10.1016/j.oneear.2021.06.008, 2021.